Noise-induced Phase Transition in an Electronic Mach-Zehnder Interferometer: a Manifestation of Non-Gaussian Noise

A. Helzel,[1] L. V. Litvin,[1] I. P. Levkivskyi,[2,3] E. V. Sukhorukov,[2] W. Wegscheider,[4] and C. Strunk[1]

[1]*Institut für experimentelle und angewandte Physik,*
Universität Regensburg, D-93040 Regensburg, Germany
[2]*Département de Physique Théorique, Université de Genève, CH-1211 Genève 4, Switzerland*
[3]*Bogolyubov Institute for Theoretical Physics, 03680 Kiev, Ukraine*
[4]*Laboratorium für Festkörperphysik, HPF E 7, ETH Zürich, 8093 Zürich, Switzerland*
(Dated: November 27, 2012)

An electronic Mach-Zehnder interferometer is employed as a detector for the non-Gaussian current noise emitted from a quantum point contact (QPC). The visibility of Aharonov-Bohm interference in the interferometer constitutes a direct probe of the generator of the full counting statistics (FCS) of the current fluctuations. The visibility shows a lobe and node structure vs. the applied dc bias, which depends on the transmission $\mathcal{T}_0$ of the QPC, and changes qualitatively at $\mathcal{T}_0 = 1/2$. The analysis of the data provides direct experimental evidence for a singularity in the FCS. The noise is highly non-Gaussian and leads to an abrupt disappearance of the multiple side lobes for $\mathcal{T}_0 < 1/2$. Together with a singularity of the dephasing rate these observations constitute an experimental evidence of a recently predicted noise-induced phase transition occurring at $\mathcal{T}_0 = 1/2$.

PACS numbers: 73.23.Ad, 73.63.Nm

Quantum noise is an important manifestation of the probabilistic nature of quantum mechanics that persists also at zero temperature. Experimental investigations of quantum noise have so far mainly concentrated on the shot noise, i.e., the variance, or second cumulant of current fluctuations.[1] For general non-Gaussian noise, further information about the statistics of current fluctuations, i.e., the full counting statistics (FCS) is contained in the higher order cumulants.[2] Only a few experimental studies of the higher order cumulants exist. Already the 3rd cumulant is usually an utterly small quantity[3,4] and measuring even higher cumulants was possible only in the special cases, where electrons can be counted one-by-one.[5,6] A direct measurement of the FCS-generator, which contains information about *all* higher cumulants of the FCS has not yet been demonstrated.

Signatures of non-Gaussian noise have been observed also via its effect on the visibility of an electronic Mach-Zehnder interferometer (MZI) with edge channels in the integer quantum Hall effect (QHE) at filling factor $ff = 2$ (see Fig. 1a,b).[7–9] Introducing noise into the copropagating inner edge channel, which was electrically disconnected from the interfering outer edge channel, was shown to reduce the visibility. A particular V-shaped dependence of the visibility ν of the interference on the transmission of the co-propagating channel was observed and attributed to the non-Gaussian character of the noise.[10] However, this observation was not reproduced in a similar experiment,[11] nor was it linked to the peculiar multiple lobe structure in $\nu(V_{dc})$ of such interferometers.

Multiple side lobes were observed experimentally in the differential visibility $\nu(V_{dc}) = (G_{max} - G_{min})/(G_{max} + G_{min})$ for a noiseless incident beam, and filling factors $2 > ff > 1.5$.[12,13] G is the differential conductance of the interferometer. Fig. 1 shows a typical sample (a), the device schematic (b), ν normalized to its value ν_0

at $V_{dc} = 0$ (c), and the corresponding phase evolution (d). To explain these side lobes several theories have been proposed.[14–20] Most of the experimental observations can be consistently explained by modelling the QHE-edge as chiral quantum wires supporting co-propagating magneto-plasmon modes. Coulomb interaction between these modes results in a pair of charged and neutral (dipolar) plasmon modes propagating at different velocities along the edge (see Fig. 1e). Because of this velocity difference charge oscillations introduced in one of the edges can be transferred from one edge to the other, resulting in a collapse of the interference pattern at certain equidistant voltages $V_m = (m - 1/2)V_0$ for a given arm length L.[18] The only free parameter in the theory is the velocity of dipole plasmons. It is reflected in a characteristic energy $\varepsilon_L = eV_0 = 2\pi\hbar v/L$ that depends on L. For two interferometers of different L, ε_L is extracted from the position of the 2nd visibility node at voltage V_2 in Fig. 1c, which corresponds to a value of $V_0 \cdot L = 2.8 \cdot 10^{-10}$ Vm, corresponding to $v = 1.1 \cdot 10^5$ m/s. For sample A (B) we obtain $\varepsilon_L = 45.8\,(30.6)\,\mu$eV.[21]

Recently, two of the authors suggested a new experimental probe to obtain *direct* information about the FCS of current fluctuations in a quantum point contact (QPC) with transparency $\mathcal{T}_0$ by coupling it to the input of a Mach-Zehnder interferometer.[22] In such an arrangement, the visibility of the interference in the interferometer turns out to be directly related to the normalized generating function $h(\lambda) = (2\pi\hbar/e^2 V_{dc}) \sum_m \langle\langle I^m \rangle\rangle (i\lambda)^m/m!$ of current cumulants $\langle\langle I^m \rangle\rangle$, while the counting field λ plays the role of a coupling constant between the two quantum systems. The generating function for a QPC[23]

$$h(\lambda) = \ln[1 + \mathcal{T}_0(e^{i\lambda} - 1)] \tag{1}$$

displays for $\lambda = \pm\pi$ a singularity at transmission $\mathcal{T}_0 = 1/2$, which in the context of quantum measurements re-
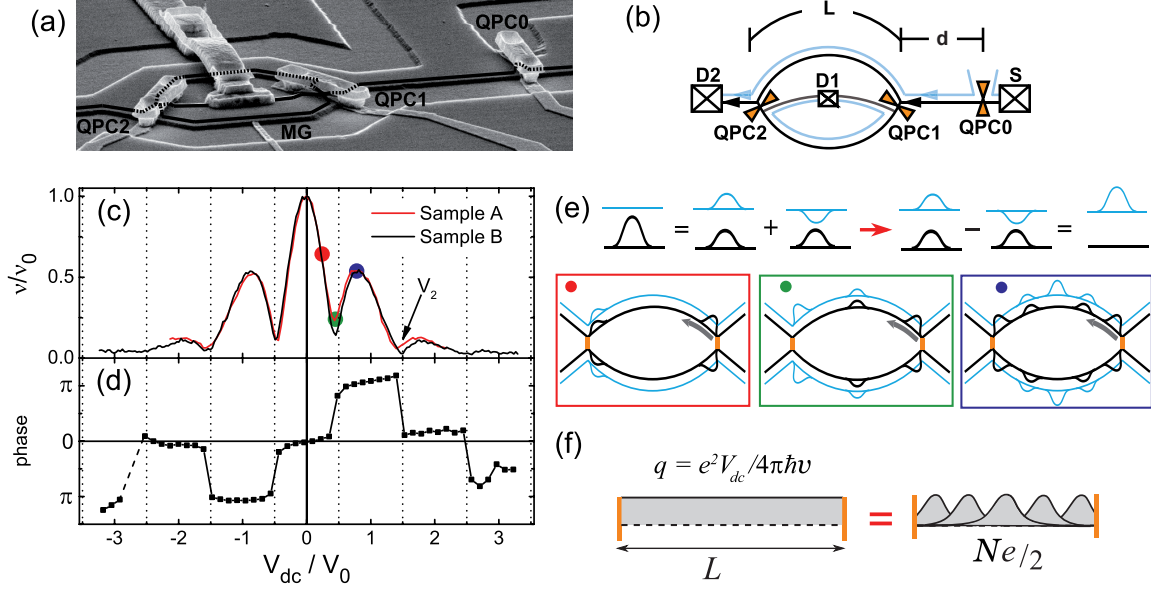
FIG. 1. **(a) Scanning electron micrograph** of the sample with marked gates QPC 0, QPC 1, QPC 2 and the modulation gate MG. The black line represents the edge channel used for the interference. QPCs 1 and 2 are set to half transmission and QPC 0 is set to transmit the outer edge with probability $\mathcal{T}_0$. Ramping the modulation gate alters the area between the electron paths and thus the Aharonov-Bohm phase. **(b) Schematic** of the edge channels in the MZI connected to source and drain. The black line is the outer edge channel carrying interfering electrons and the light blue line represents the inner edge channel. **(c) Multiple lobe structure:** If a dc voltage is applied to the interfering edge channel [black line in panels (a, b)] the differential visibility shows a multiple lobe structure with several nodes, which is displayed for two samples, A (red line) and B (black line). When scaling the visibility with respect to the zero bias maximum visibility ν_0 and the voltage with respect to the node spacing V_0 the curves of the two samples collapse. **(d)** The **phase evolution** The lobes are reflected as phase-rigid plateaus within the lobes and phase jumps of π at the nodes. **(e) Illustration of charged and dipole plasmons**: An electron tunnelling through QPC1 excites plasmon wave packets, i.e., a superposition of charged and dipolar plasmon modes. At QPC2 the charge- and dipole-plasmons acquired a relative phase shift (see Eq. 4) that transfers the plasmon wave-packet to the unbiased edge channel (blue line), where it cannot interfere with the companion wave-packet travelling in the other interferometer arm.[26] The plasmon wave-packets leaving the interferometer via the unbiased channels contribute with a weight set by the transparency of QPC1 in both detector terminals, and hence reduce the visibility ν [left panel (•), $V_{dc} = V_0/2$] until it reaches a node [middle panel (•), $V_{dc} = V_0$]. At $V_{dc} = 3V_0/2$ [left panel (•)] the wave-packets are recollected at QPC2 and the visibility is partially recovered. **(f) Illustration of the origin of the electrostatic phase shift**: A spatially homogeneous charge density $q = -Ne/(2L)$ is accumulated at the outer edge channel in the upper arm of the interferometer. The corresponding electric potential leads to a homogeneous shift of the energies in the channel. The spatial shift of the biased edge caused by the accumulated charge density results in an electrostatic phase shift of π (see Eq. 5) in the charge component of the wave function.

flects perfect entanglement between the MZI and the QPC as a consequence of the strong coupling between the two.[24]

In this article, we the investigate signature of the full counting statistics of current fluctuations of a quantum point contact, directly coupled to the interfering edge channel of a Mach-Zehnder interferometer. We exploit the sensitivity of the multiple lobe structure of ν to the noise in the incoming beam, and present experimental evidence for a new type of noise induced non-equilibrium phase transition that was predicted to occur at $\mathcal{T}_0 = 1/2$.[22] The singularity in the full counting statistics (Eq. 1) is reflected in an abrupt transition from a regime with multiple side lobes, with V_0-periodic oscillations in the visibility $\nu(V_{dc})$ to a regime with only *one* node. The dephasing rate is strongly peaked at the tran-

sition point $\mathcal{T}_0 = 1/2$. The theory describes the observed variations of $\nu(V_{dc})$ very well, and gives a quantitative account for the shift of the visibility nodes V_m as function of $\mathcal{T}_0$.

The results are obtained on two samples made from different wafers. Sample A was structured in a modulation doped GaAs/Ga$_x$Al$_{1-x}$As heterostructure with a two dimensional electron gas (2DEG) 90 nm below the surface. The 2DEG density and mobility are $n = 2 \times 10^{15}$ m^{-2} and $\mu = 206$ m^2/(Vs) ($\mu = 289$ m^2/(Vs) in sample B) at 4 K on the unpatterned wafer. The exact patterning procedure is described in Ref. 9. The arm's length L of the interferometers is estimated to be 6.5 μm for sample A and 8.7 μm for sample B. The structures contain not only the MZI, i.e. QPC 1 and 2 and two drains, but also an additional quantum point contact (QPC0)

between source and MZI. This QPC0 is situated a distance $d = 5\,\mu$m for sample A and $8\,\mu$m for sample B in front of QPC 1 (see Fig. 1a). A standard lock-in technique ($f \sim 300\,$Hz) was used to measure the output current via voltage drop between terminal D2 and another (grounded) ohmic contact. An ac voltage of $1\,\mu$V plus a dc voltage V_{dc} were applied to measure the differential conductance $G(V_{dc}) = dI(V_{dc})/dV_{dc}$. We employed noise thermometry, to ensure that the electron temperature in the interferometer is close to the bath temperature.[25] Sample A was measured at a magnetic field of $4.73\,$T ($ff = 1.7$) and with ideal configuration of the QPCs a (maximum) visibility of 65 % at $V_{dc} = 0$ is achieved, sample B at $4.5\,$T ($ff = 1.8$) with a maximum visibility of 33.5 %.

In order to elucidate the relation between the FCS and the interferometer visibility, let us briefly summarize the theory of Refs. 18 and 22 in elementary terms: the state of the interferometer is given by a product of charge and plasmon components, and changes upon the entrance of a quasiparticle at QPC1 as

$$|\psi_N\rangle = |N\rangle \rightarrow |\psi_{N+1}\rangle = |N+1\rangle|\text{plasmons}\rangle, \quad (2)$$

where

$$N = \frac{eV_{dc}}{\varepsilon_L} = \frac{eV_{dc}L}{2\pi\hbar v}, \quad (3)$$

is the number of excess quasiparticles in the interferometer, and the plasmon state is a superposition of charged, and dipole modes $|\text{plasmons}\rangle = (|\text{charged}\rangle + |\text{dipole}\rangle)/\sqrt{2}$. We assume that the group velocity v of the dipole mode is much smaller than that of the charge mode. As we show next, this implies that v and the corresponding energy scale $\varepsilon_L = 2\pi\hbar v/L$ enters both the phase shift between charge and dipole excitations, and the quantum capacitance of the channels.

Upon propagation towards QPC2 the plasmon component of $|\psi_{N+1}\rangle$ undergo a dynamical evolution, i.e.

$$|\text{plasmons}'\rangle = \frac{|\text{charged}\rangle + \exp(i2\pi N)|\text{dipole}\rangle}{\sqrt{2}} \quad (4)$$

with a dynamical phase shift $2\pi N = eV_{dc}L/(\hbar v)$ of the dipole mode excited at energy eV_{dc}. On the other hand, the charge component

$$|N+1'\rangle = \exp(-i\pi N)|N+1\rangle, \quad (5)$$

acquires an electrostatic phase shift of $-\pi N = (-e/2)V_{dc}L/(\hbar v)$, because the excess charge $(-e/2)N = C_q V_{dc}$ per channel corresponding to an excess of N quasiparticles in the interferometer, is related to the voltage bias V_{dc} via the quantum capacitance $C_q = e^2 Lg(\varepsilon) = e^2/(\pi\varepsilon_L)$, where $g(\varepsilon)$ is the density of states of the one-dimensional channel. Both phase shifts can thus be expressed in terms of N (see Eq. 3). Combining the charge and plasmon sector the total overlap of the wave functions $|\psi_{N+1}\rangle$ and $|\psi_{N+1}\rangle'$ reads:

$$\langle\psi_{N+1}|\psi'_{N+1}\rangle = e^{-i\pi N} \cdot \frac{1+e^{i2\pi N}}{2} = \cos(\pi N). \quad (6)$$

This result explains the periodicity and phase rigidity of the lobe pattern observed in Fig. 1d.

In Fig. 1c a strong damping of the oscillations is seen that has been phenomenologically accounted for by an additional factor $D(V_{dc}) = \exp(-(eV_{dc})^2/2\varepsilon_0^2)$ in Ref. 13 with a characteristic energy ε_0 that is of the same order of magnitude as ε_L. The damping is an effect of inelastic scattering,[27] which is not contained in the theory. In the following it will be removed by normalizing the visibility $\nu(V_{dc}, \mathcal{T}_0)$ with respect to $\nu(V_{dc}, \mathcal{T}_0 = 1)$.

The essential point is now that the overlap of interfering quantum states in Eq. 6 depends on the number of excess quasi-particles in the interferometer, which is equal to N for $\mathcal{T}_0 = 1$. If the transparency $\mathcal{T}_0$ of QPC0 is reduced below one, this number becomes a random variable n, which fluctuates according to the binomial statistics between 0 and N with the average value $\langle n\rangle = \mathcal{T}_0 N$. To find the visibility of the interference pattern ν one needs to average the overlap $\langle\psi_{n+1}|\psi'_{n+1}\rangle$ over the possible particle numbers:

$$\nu = \left|\sum_{n=0}^{N} P(N,n)\cos(\pi n)\right| = \left|\text{Re}\exp[N\cdot h(\pi)]\right|, \quad (7)$$

where $N\cdot h(\lambda) \equiv \ln\left[\sum_0^N P(N,n)e^{i\lambda n}\right]$ is the cumulant generating function of the binomial distribution $P(N,n) = B_N^n \mathcal{T}_0^n(1-\mathcal{T}_0)^{N-n}$, and B_N^n being the binomial coefficients. Hence, *the generator of the QPC's FCS is directly related to the visibility of the interfering currents*. The evaluation of the sum in Eq. 7 results in:

$$\nu = \left|\cos[N\cdot\Theta(2\mathcal{T}_0-1)]\right|\cdot\exp\left[N\cdot\ln|2\mathcal{T}_0-1|\right], \quad (8)$$

where Θ is the Heaviside step function, and the non-analytic structure of ν stems from the singularity in $h(\lambda)$ at $\lambda = \pi$ and $\mathcal{T}_0 = 1/2$. This is the origin of the noise-induced phase transition predicted in Ref. 22.

The result in Eq. 8 contains an oscillatory and a dephasing factor, which both depend on N and $\mathcal{T}_0$. For $\mathcal{T}_0 > 1/2$ multiple side lobes are expected, with visibility nodes that remain independent of V_{dc}. For $\mathcal{T}_0 < 1$ the normalized visibility is exponentially damped at large V_{dc}. From the logarithm in the dephasing term in Eq. 8 one expects a divergence of the dephasing rate at $\mathcal{T}_0 = 1/2$. The more rigorous treatment in Ref. 22 and our numerical calculations (see supplementary material) take into account the quantum fluctuations of n and result in a divergence of the oscillation period, when $\mathcal{T}_0$ approaches $1/2$.

In the following, we show that all of these rich and intriguing predictions are observable in our experiment, and provide clear evidence for the non-Gaussian character of the noise. In Fig. 2 we present the evolution of the lobe pattern when we introduce noise to the interfering edge channel of the MZI by closing QPC0 (see the inset in Fig. 2) so that the outer edge channel is only partially transmitted. For $\mathcal{T}_0 \geq 0.5$ the number and position of the visibility nodes, stays (almost) constant, while the
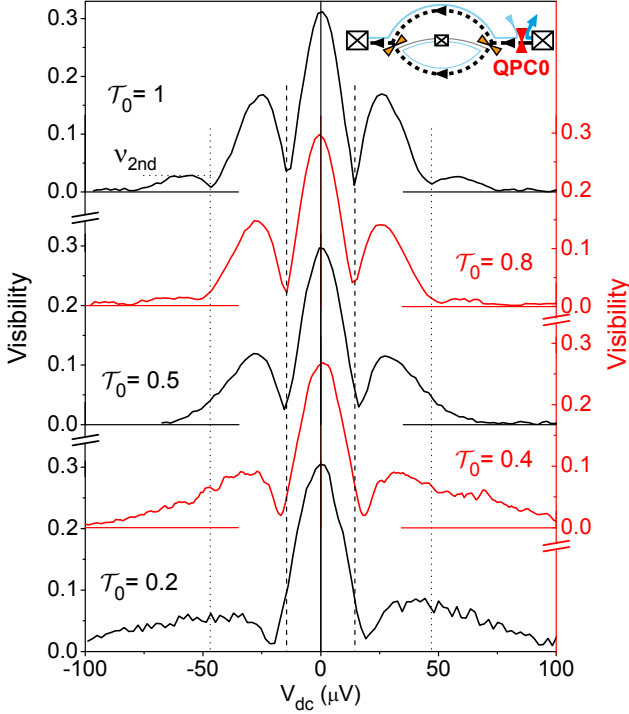
FIG. 2. **Visibility lobe structure of sample B** ($L = 8.7\,\mu$m) **for different** $\mathcal{T}_0$: When closing QPC 0 (see inset) below $\mathcal{T}_0 = 1$ the node positions remain essentially unchanged for transmissions $\mathcal{T}_0 \geq 0.5$, i.e., multiple side lobes with the same widths of lobes and position of nodes as for $\mathcal{T}_0 = 1$. The lobe height is strongly reduced at finite dc bias. Below $\mathcal{T}_0 = 1/2$ the lobe structure changes from the multiple side lobe behavior to a single side lobe behavior. The central lobe width increases with decreasing transmission and the first side lobes are stretched to large bias.

height of the second side lobe is gradually suppressed. The number of the side lobes and the phase rigidity is more clearly seen in the derivative $d\varphi(V_{\mathrm{dc}})/dV_{\mathrm{dc}}$ of the phase plotted in Fig. 3. Close to $\mathcal{T}_0 \simeq 0.5$ a second node is hard to see in Fig. 2, but a drop to zero visibility and the phase jump is still apparent in the gate modulation of the MZI-current in Fig. 3. Some structure is also seen at $\mathcal{T}_0 = 0.5$ (see supplementary material).

The situation changes drastically for $\mathcal{T}_0 \leq 0.5$ when multiple nodes and multiple side lobes disappear abruptly. This is seen very clearly in Fig. 3. The central lobe width is increasing with decreasing QPC0 transmission, i.e., the remaining single phase step shifts to high voltages and no additional nodes can be seen (see Fig. 2).

Next we present a detailed and quantitative comparison of dependence of the measured position of the visibility nodes and the height of the second side lobe on $\mathcal{T}_0$ with numerical calculations (see supplementary material) that extend the predictions of Ref. 22. In Fig. 4a we plot the positions V_m of the first three visibility nodes vs. $\mathcal{T}_0$ for sample B. For $\mathcal{T}_0 = 1$ these are expected at $V_m = (m-1/2)\,\varepsilon_L/e$. Only the first visibility node is ob-
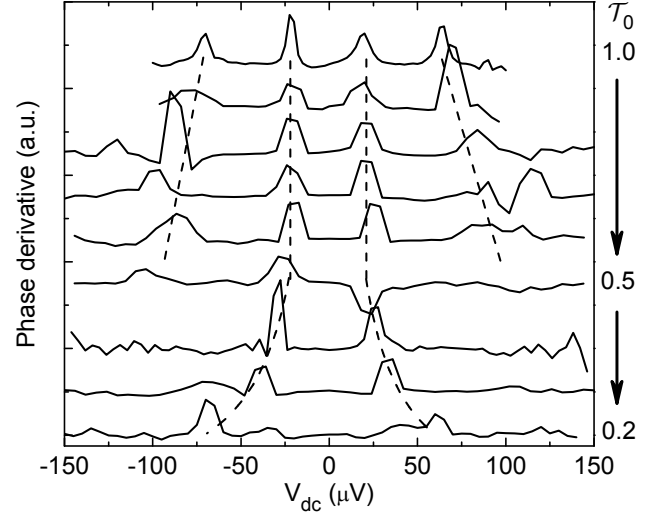

FIG. 3. **Phase changes of sample A** ($L = 6.5\,\mu$m) **for different** $\mathcal{T}_0$: As in Fig. 1d the phase evolution shows steps at visibility nodes, which become more discernible as peaks. Curves show the numerical derivative $d\varphi(V_{\mathrm{dc}})/dV_{\mathrm{dc}}$ of the phase for different transmission of QPC0 (from 1.0 to 0.2 in steps of 0.1). The width of the inner pair of phase steps remains nearly fixed for $\mathcal{T}_0 > 0.5$. Upon a further decrease of $\mathcal{T}_0$ the width of the central lobe is increasing.

served in the whole range of transparencies $0.1 \leq \mathcal{T}_0 \leq 1$. The presence of the 2nd and 3rd visibility node is limited to the range $0.5 \leq \mathcal{T}_0 \leq 1$, as predicted for non-Gaussian noise only. For decreasing transparency $\mathcal{T}_0$ the nodes shift outward in a way that is captured quantitatively by our numerical calculations (full lines) when using the value for the velocity of dipolar plasmons determined from Fig. 1c. The dashed lines arise, when Gaussian noise is modelled by truncating the Taylor expansion of the FCS-generator (Eq. 1) in λ after the quadratic term. In this case, a stronger variation of all visibility nodes with $\mathcal{T}_0$ is expected, and the 2nd and 3rd node should exist also below $\mathcal{T}_0 = 0.5$. The observed absence of visibility nodes with $m > 1$ is thus strong evidence for the non-Gaussian character of the noise. The position of the 1st visibility node is slightly reduced with respect to the expected value $\varepsilon_L/2e$.

According to our theory, the amplitude of the second side lobe $\nu_{2\mathrm{nd}}(\mathcal{T}_0)$ vanishes in a universal quasi-linear fashion near $\mathcal{T}_0 = 0.5$, i.e., it is independent of the system parameters v and L. In Fig. 4b we present the ratio $\nu_{2\mathrm{nd}}(\mathcal{T}_0)/\nu_{2\mathrm{nd}}(\mathcal{T}_0 = 1)$ of the maximal visibility amplitudes $\nu_{2\mathrm{nd}}(\mathcal{T}_0)$ determined form sweeps of the modulation gate. The normalization with respect to $\nu_{2\mathrm{nd}}(\mathcal{T}_0 = 1)$ is necessary, to divide out the additional dephasing factor $D(V_{\mathrm{dc}})$ discussed above. Within the limits of the experimental accuracy, our data are again in good agreement with the theory.

In order to illustrate the character of the transition, and demonstrate the agreement of the measured data
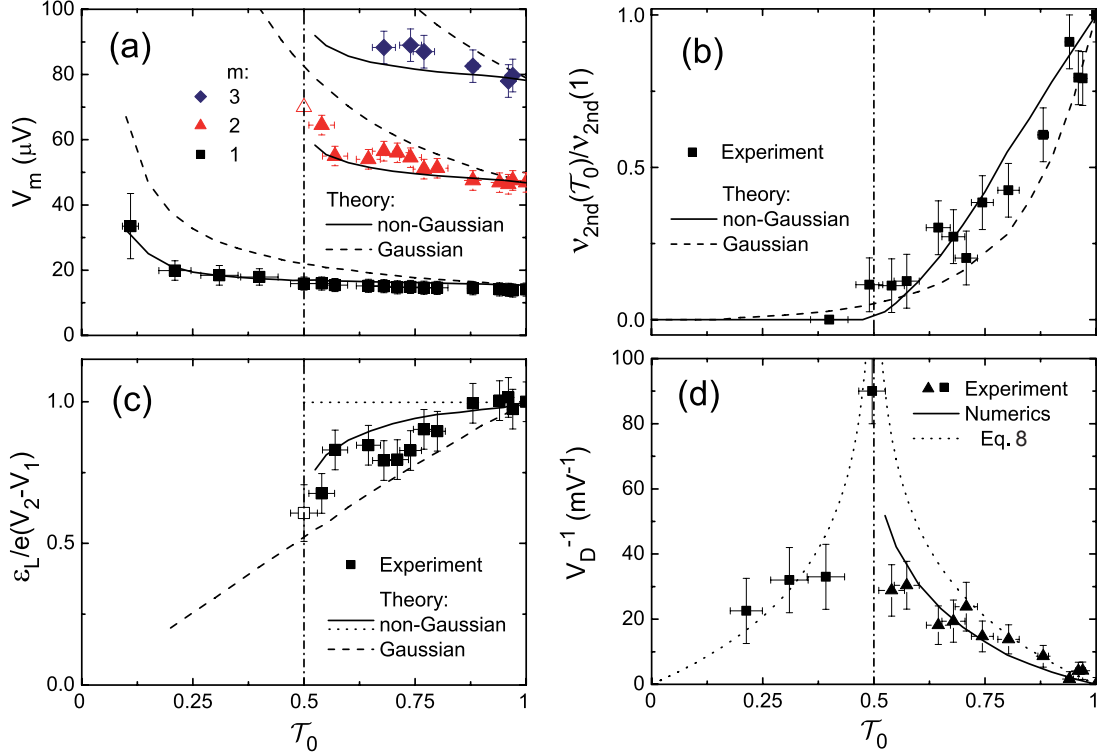
FIG. 4. **Nodes, lobes, and the phase transition: (a)** Dots: Measured visibility node positions V_m vs. the transparency of QPC0. The nodes shift outward, and disappear for $m > 1$ at $\mathcal{T}_0 = 1/2$. Solid lines: Predictions of the full theory using the characteristic energy $\varepsilon_L = 30.6\,\mu$eV extracted from Fig. 1c. Dashed lines: Gaussian approximation of the theory. **(b)** Dots: Maximal visibility ($\nu_{2\mathrm{nd}}$) of the second side lobes [see Fig. 2 (sample B)], normalized with respect to $\nu_{2\mathrm{nd}}(\mathcal{T}_0 = 1)$. Solid (dashed) line: theoretical prediction for the full theory (its Gaussian approximation). While the Gaussian approximation predicted multiple side lobes for all values of $\mathcal{T}_0$, they appear in the full theory only for $\mathcal{T}_0 = 0.5$. **(c)** Inverse normalized node spacing $e(V_2 - V_1)/\varepsilon_L$ as a signature of the non-equilibrium phase transition. Full line: full numerical calculation of the node spacing. Dotted line: expectation from the approximation of Eq. 3. Dashed line: Gaussian approximation of the full theory. The dash-dotted line indicates the point of the phase transition. In presence of non-Gaussian noise the inverse node spacing vanished abruptly at the transition point $\mathcal{T}_0 = 1/2$. **(d)** Dephasing rate V_D^{-1} extracted from the exponential decay of $\nu(V_{\mathrm{dc}})$ in Fig. 2 for $\mathcal{T}_0 \le 1/2$ (squares) and the amplitude of the $\nu_{2\mathrm{nd}}(V_{\mathrm{dc}})$ in (b) for $\mathcal{T}_0 > 1/2$ (triangles). The dotted line represents the dephasing rate extracted from Eq. 8, while the solid line is the result of the numerical simulations. No free parameters are adjusted in the theory curves of all four panels.

with the structure of Eq. 8 we display the peculiar variation of the arguments of the cos and exp-factors in Eq. 8 vs. $\mathcal{T}_0$. Figure 4c shows the variation of the inverse node spacing $\varepsilon_0/[e(V_2 - V_1)]$ extracted from Fig. 4a. Instead of a step function (dotted line) expected from the elementary argument leading to Eq. 8, a rounding of the step is found that results from quantum fluctuations of N and agrees well with our numerical calculation (full line). On the other hand, the Gaussian truncation of the FCS predicts a linear decay from 1 to 0 (dashed line) rather than a step. Again, the absence of higher visibility nodes below $\mathcal{T}_0 = 1/2$ demonstrates the essential contribution of the higher cumulants contained in Eq. 1. Moreover, the abrupt decay of $\varepsilon_0/[e(V_2 - V_1)]$ at the transition point $\mathcal{T}_0 = 1/2$ suggest to consider this quantity as a normalized order parameter for the non-equilibrium phase transition predicted in Ref. 22.

In Fig. 4d we display the peaked behavior of the de-

phasing rate $V_D^{-1}(\mathcal{T}_0) = (e/2L) \cdot \ln|2\mathcal{T}_0 - 1|$ defined by Eq. 8. The points were extracted from from Fig. 4b for $\mathcal{T}_0 > 0.5$, and the exponential tails of $\nu(V_{\mathrm{dc}})$ in Fig. 2 for $\mathcal{T}_0 \le 0.5$. We see that $V_D^{-1}(\mathcal{T}_0)$ shows indeed a pronounced peak at the transition point $\mathcal{T}_0 = 0.5$ which decays in a way that is quantitatively reproduced by the theory, using again the same value for the velocity of dipolar plasmons determined from Fig. 1c. The singular dephasing rate at the transition point reflects the dominance of the non-Gaussian noise at the non-equilibrium phase transition.

In conclusion, our work constitutes a detailed investigation of the effect of non-Gaussian noise on the visibility of interference in electronic interferometer. The lobe- and node structure of the visibility directly reflects the peculiar analytic structure of the generator of the full counting statistics of a quantum point contact. It provides first experimental evidence of a singularity in

the FCS that is intrinsic to binomial statistics, and that induces a novel type of non-equilibrium phase transition. In addition, the excellent overall agreement of the observed behavior of the visibility with the predictions of the plasmonic edge model provides firm evidence that the latter captures the essential physics behind the complex interference phenomena observed in Mach-Zehnder interferometers with two co-propagating edge channels.

[1] Ya. M. Blanter and M. Buttiker, *Phys. Repts.* **336**, 1 (2000).

[2] Yu. V. Nazarov (Edt.), *Quantum Noise in Mesoscopic Physics*, (Kluwer, Dordrecht 2003).

[3] B. Reulet, J. Senzier, and D. E. Prober *Phys. Rev. Lett.* **91**, 196601 (2003).

[4] G. Gershon, Yu. Bomze, E. V. Sukhorukov, and M. Reznikov *Phys. Rev. Lett.* **101**, 016803 (2008).

[5] S. Gustavsson, R. Leturcq, B. Simovic, R. Schleser, T. Ihn, P. Studerus, K. Ensslin, D. C. Driscoll, and A. C. Gossard, *Phys. Rev. Lett.* **96**, 076605 (2006); S. Gustavsson, R. Leturcq, B. Simovic, R. Schleser, T. Ihn, P. Studerus, K. Ensslin, D. C. Driscoll, A. C. Gossard, *Phys.Rev.* B **74**, 195305 (2006).

[6] C. Flindt, C. Fricke, F. Hohls, T. Novotny, K. Netocny, T. Brandes, and R. J. Haug, *PNAS* **106**, 10116 (2009); C. Fricke, F. Hohls, N. Sethubalasubramanian, L. Fricke, R. J. Haug *Appl. Phys. Lett.* **96**, 202103 (2010).

[7] Y. Ji, Y. Chung, D. Sprinzak, M. Heiblum, D. Mahalu, and H. Shtrikman, *Nature* **422**, 415 (2003).

[8] P. Roulleau, F. Portier, D. C. Glattli, P. Roche, A. Cavanna, G. Faini, U. Gennser, and D. Mailly, *Phys. Rev. B* **76**, 161309(R) (2007).

[9] L. V. Litvin, H.-P. Tranitz, W. Wegscheider, and C. Strunk, *Phys. Rev. B* **75**, 033315 (2007).

[10] I. Neder, F. Marquardt, M. Heiblum, D. Mahalu, and V. Umansky, *Nat. Phys.* **3**, 534 (2007).

[11] P. Roulleau, F. Portier, P. Roche, A. Cavanna, G. Faini, U. Gennser, D. Mailly, *Phys. Rev. Lett.* **101**, 186803 (2008).

[12] I. Neder, M. Heiblum, Y. Levinson, D. Mahalu, and V. Umansky, *Phys. Rev. Lett.* **96**, 016804 (2006).

[13] L. V. Litvin, A. Helzel, H.-P. Tranitz, W. Wegscheider, and C. Strunk, *Phys. Rev. B* **78**, 075303 (2008).

[14] V. Cheianov and E. V. Sukorukov, *Phys. Rev. Lett.* **99**, 15680 (2007).

[15] J. T. Chalker, Yu. Gefen, and M. Y. Veillette, *Phys. Rev. B* **76**, 085320 (2007).

[16] I. Neder and E. Ginossar, *Phys. Rev. Lett.* **100**, 196806 (2008).

[17] S.-C. Youn, H.-W. Lee, and H.-S. Sim, *Phys. Rev. Lett.* **100**, 196807 (2008).

[18] Ivan P. Levkivskyi, Eugene V. Sukhorukov, *Phys.Rev.* B **78**, 045322 (2008).

[19] D. L. Kovrizhin and J. T. Chalker, *Phys. Rev. B* **80**, 161306 (2009); *ibid.* **81**, 155318 (2010).

[20] M. Schneider, D. Bagrets and A. Mirlin, *Phys. Rev. B* **84**, 075401 (2011).

[21] This definition of ε_L agrees with that of Ref. 13, and differs from that of Ref. 22 by a factor of 2π.

[22] I. P. Levkivskyi, E. V. Sukhorukov, *Phys. Rev. Lett.* **103**, 036801 (2009).

[23] L. S. Levitov, H. Lee, G. B. Lesovik, *J. Math. Phys.* **37**(10), 4845 (1996).

[24] D. V. Averin and E. V. Sukhorukov, *Phys. Rev. Lett.* **95**, 126803 (2005).

[25] M. Hashisaka, A. Helzel, S. Nakamura, L. V. Litvin, Y. Yamauchi, K. Kobayashi, T. Ono, H.-P. Tranitz, W. Wegscheider, and C. Strunk, Physica E **42**, 1091-1094 (2010).

[26] The oscillation of the plasmon wave packets between the two edge channels is very similar to the neutrino oscillations phenomenon in the high energy physics. In our situation, the flavor eigenstates of neutrinos correspond to plasmons excitations in the inner and outer channels, while the mass eigenstates of neutrinos correspond to the charged and dipole plasmons. See, e.g., B. Pontecorvo, Sov. Phys. JETP **26**, 984 (1968).

[27] C. Altimiras, H. le Sueur, U. Gennser, A. Cavanna, D. Mailly, and F. Pierre, *Nature Physics* **6**, 34 (2010).

Supplementary information for "Noise-induced Phase Transition in an Electronic Mach-Zehnder Interferometer: a Manifestation of Non-Gaussian Noise"

I. ANALYSIS

We measured $dI/dV_{dc} = G$ vs. V_{dc} for a range of modulation gate voltage V_{mg}. An example of raw data can be seen in Fig. S5a. The sinusoidal oscillations for ramping V_{mg} and the decaying oscillations for V_{dc} are well-defined. In the raw data the multiple side lobes can be seen as a chess board pattern that fades out at larger V_{dc}. We extract the visibility

$$\nu(V_{dc}) = \frac{G_{max}(V_{dc}) - G_{min}(V_{dc})}{G_{max}(V_{dc}) + G_{min}(V_{dc})} \qquad \text{(S9)}$$

of the interference pattern at each bias voltage V_{dc} (Fig. S5b). The Aharonov Bohm phase and the visibility in Fig. 2 of the main part are determined from sine fits of modulation gate traces at certain V_{dc} relative to the trace at zero bias (Fig. S5c).

We fit the measured modulation gate traces to

$$G(V_{mg}) \;=\; G_{av} + G_{osc} \sin(V_{mg}/V_p + \Delta\varphi) \qquad \text{(S10)}$$
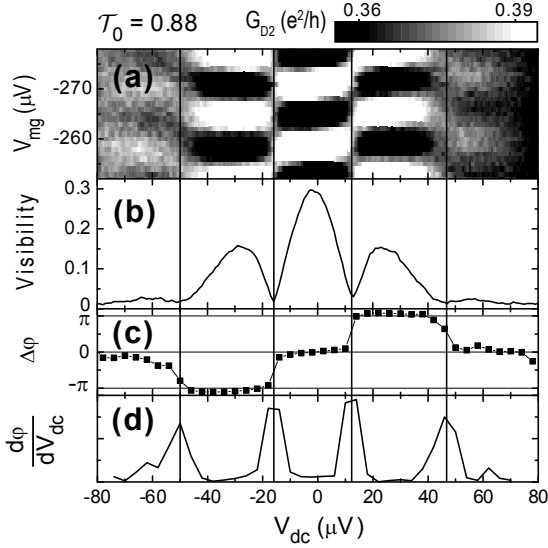

FIG. S5. **Raw and processed data:** (a) Gray scale plot of the measured conductance $G(V_{dc}, V_{mg})$ for $\mathcal{T}_0 = 0.88$. Checker-board pattern of dark and bright regions reveals central lobe and two additional lobes on each side. (b) The visibility of the in (a) measured oscillatory conductance extracted according to Eq. S9. (c) The AB-phase shift $\Delta\varphi$ with respect to $V_{dc} = 0$ obtained from fits of traces $G(V_{mg})$ with Eq. S10. Constant phase inside lobes and jumps of π at nodes can be seen. (d) The numerical derivative of φ further highlights the position of the nodes as pronounced peaks.
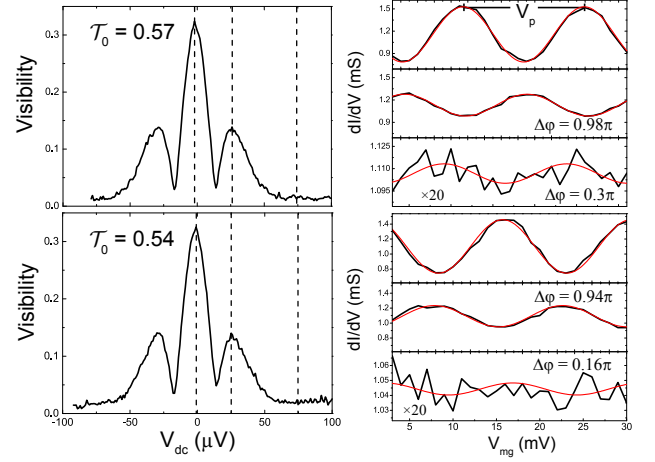

FIG. S6. **Sine fits of gate traces:** On the left the visibilities vs. V_{dc} for $T_{QPC0} = 0.57$ (top) and 0.54 (bottom) are displayed. On the right are according modulation gate traces (black line) of the marked V_{dc} (dashed vertical lines in the left plots) at the center of the lobes and their sine fits (red line). For $V_{dc} \approx 75\,\mu V$ only residual oscillations buried in noise are present.

with the four parameters G_{av}, G_{osc}, V_p, and $\Delta\varphi = \varphi(0) - \varphi(V_{dc})$. For a measurement of each transmission $\mathcal{T}_0$ we fit the period V_p only once for the large oscillations at zero bias and then keep it fixed for the other traces of one measurement. Examples of typical modulation gate traces and the corresponding fit curves can be seen in Fig. S6 for transmissions 0.57 and 0.54. In this way we trace the phase evolution at the frequency of interest even if it is nearly buried in noise. This becomes crucial for very small oscillation amplitudes. From such fits we determined ν_{2nd} in Fig. 4b of the main part for transmissions $\mathcal{T}_0$ close to 0.5.

Fig. S5d shows the numerical derivative of $\varphi(V_{dc})$ to highlight the phase jumps at the nodes, as it is used in Fig. 3, main part. For the evaluation of the node positions V_m and the height of the second side lobe in Fig. 4 of the main part, both visibility and phase evolution are analyzed to determine the node positions.

II. CHARACTERIZATION OF THE INTERFEROMETERS:

Two samples are studied, which differ in interferometer arm length L and distance d (see Methods). The maximal two-terminal conductance is $\approx 2e^2/h$, corresponding to two transmitted edge channels. We use QPC0 to selectively bias the outer edge channel, while the source terminal of the inner channel is left grounded ($\mathcal{T}_0 = 1$). QPCs 1 and 2 are set to reflect the inner channel, implying that the interference takes place only in the outer edge channel. At zero bias we reach maximal interference visibilities (ν_0) of 65 % in sample A and 33.5 % in

sample B. Besides the maximum visibility ν_0 the lobe periodicity V_0 is different for the samples. Both parameters depend on the magnetic field, the temperature and the arm length L of the interferometer.[2,4,5]

The visibility ν_0 at zero dc bias decreases exponentially with L, $\nu \propto \exp(-2L/l_\varphi)$, with the coherence length $l_\varphi \propto T^{-1}$, similar to the data in Refs. 4 and 2. The different maximum visibilities of the two samples result from the different sizes L, affecting both ν_0 and V_0. The normalized visibility pattern $\nu(V_{dc}/V_0)/\nu_0$ in Fig. 1c of the main part turns out to be independent of L. We can conclude that for $\mathcal{T}_0 = 1$ the differences between both samples are controlled by only one parameter, i.e., the L-dependent characteristic energy $\varepsilon_L = 2\pi\hbar v/L$. The presence of visibility nodes is even more clearly visible in the evolution of the Aharonov-Bohm phase. In the visibility only two side lobes can be seen clearly, whereas the analysis of the residual oscillations at high bias voltages by sinusoidal fitting (see methods) display one more phase jump, revealing a third side lobe in sample B.

III. COMPARISON OF SAMPLES A AND B

In the main part we mainly display data obtained on sample B. Here we present an overview of the lobe structure for sample A in Fig. S7. The qualitative behavior in sample A is similar to sample B, i.e., the positions V_m of the multiple side nodes (see Fig. S7a) and the phase jumps (see Fig. S7b) remain fixed for $\mathcal{T}_0 > 0.5$ and the location V_1 of the single side node increases for $\mathcal{T}_0 < 0.5$. Such behavior is also seen in the numerical derivative of $\varphi(V_{dc})$ (Fig. 3 of the main part). For $\mathcal{T}_0 = 1$ we can match the visibility curves for the two samples very well by normalization with respect to the node spacing V_0 and the zero-bias visibility ν_0 (see Fig. 1c in the main part).

In contrast, for lower transmissions $\mathcal{T}_0 < 1$ of QPC0 differences between sample A and B remain, which originate from the operation of QPC0 as a source of current noise at the interferometer input. In Fig. S8 the discrepancies are shown for two exemplary transmissions $\mathcal{T}_0 = 0.7$ and $\mathcal{T}_0 = 0.2$. The voltages are scaled with respect to $2V_1$ extracted from the trace with $\mathcal{T}_0 = 1$. The measurement of the phase shift in Fig. S7b allows an unambiguous determination of the node positions V_m, which are marked by the dashed lines in Fig. S8. Because of the scaling the first visibility nodes match, but the second visibility nodes disagree for $\mathcal{T}_0 = 0.7$. Moreover, even the first visibility nodes of the two samples do not collapse for $\mathcal{T}_0 = 0.2$. In addition, a foot develops in ν near $V_{dc} \lesssim V_1$.

The overall variation of V_1 vs. $\mathcal{T}_0$ for both samples is shown in Fig. S9 together with theory curves for the Gaussian and non-Gaussian case. For lower transmissions the shift of V_1 with transmission is much stronger for sample A, when compared with sample B. Below $\mathcal{T}_0 = 0.5$ a cross-over from non-Gaussian to Gaussian behavior is observed for sample A. This observation can be
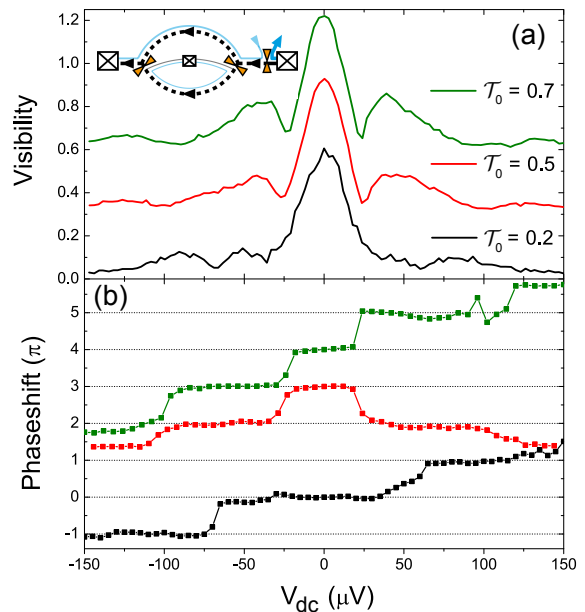

FIG. S7. **Evolution of the lobe structure in sample A:** Visibility (a) and phase shift (b) vs. dc bias voltage for various transmissions of QPC0 for sample A. For $\mathcal{T}_0 \geq 0.5$ multiple side lobes are present in the visibility and the phase evolution, similar to sample B. For $\mathcal{T}_0 = 0.2$ we see a wide central lobe and only single side lobes. The position of the nodes is clearly visible in the phase behavior by jumps and we can deduce the lobe structure.

made plausible by the following argument: at finite voltages the statistics of the particle numbers transmitted through QPC0 is expected to be non-Gaussian.[7] It was shown in Ref. 8, however, that a weak non-linearity in the spectrum of the plasmon modes $k(\omega) = \omega/v + \gamma\omega^2\text{sign}(\omega)$ can suppress the contributions of higher order cumulants in the FCS generator for distances $L_g = 1/(\gamma T V_{dc})^2$ that strongly depend on the bias voltage V_{dc}. Such a non-linear plasmon dispersion relation can also lead to a non-linear conductance of the QPC. A cross-over to Gaussian noise can result from a decrease of $L_g(V_{dc})$ with larger V_{dc}, or from sufficiently strong nonlinearity of the plasmon dispersion relation in sample A, which ensure $L_g < d$ already at small voltages. We checked carefully that sample B shows negligible nonlinearities in the current-voltage-characteristic of the QPCs. This is consistent with the observed non-Gaussian behavior of the visibility. On the other hand, we found that sample A has strong nonlinearities in the conductance. Because the arm length L of interferometer A is smaller, the important energy ε_L and thus the required voltages V_m are larger in sample A (the ratio L/d is similar in both samples). Together with the strong voltage dependence of L_g this may explain the observed cross-over from non-Gaussian to Gaussian behavior of V_1 for $\mathcal{T}_0 < 0.5$ and V_2 for $\mathcal{T}_0 > 0.5$ in Figs. S8 and S9. The larger characteristic energy ε_L of sample A makes it more prone to a suppres-
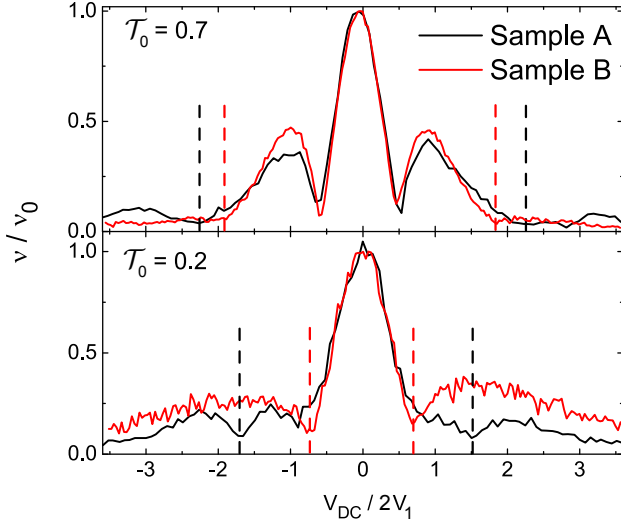
FIG. S8. **Differences between samples A and B:** The visibility for $\mathcal{T}_0 = 0.7$ and $\mathcal{T}_0 = 0.2$ of both samples are shown. The dashed lines mark the position of the second nodes (upper panel) and first nodes (lower panel) for sample A (black) and B (red). Though for $\mathcal{T}_0 = 1$ the curves for sample A and B coincide after scaling by ν_0 and V_0, this is different for lower transmission of QPC0.
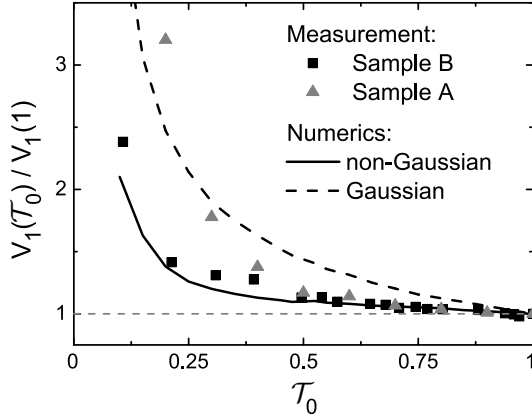

FIG. S9. **Evolution of $V_1(\mathcal{T}_0)$:** The position of the first node V_1 follows the non-Gaussian prediction for large $\mathcal{T}_0$. For transmissions $\mathcal{T}_0 < 0.5$ the voltage V_1 of the first visibility node (dots) grows more rapidly for sample A than for sample B, indicating a cross-over from non-Gaussian (solid line) to Gaussian (dashed line) behavior, in particular for sample A.

sion of higher order cumulants at larger voltages, when compared with sample B. From Ref. 5 it is expected that there are no multiple side lobes at $\mathcal{T}_0 = 0.5$. In contrast to this prediction we observe traces of a second side lobe in our experimental data at $\mathcal{T}_0 = 0.5$, in particular for sample A (see Fig. S7 and Fig. 2, main part). Fig. S10 shows the measured phase shifts for both samples at this point. After the jump of the phase from 0 to π at the
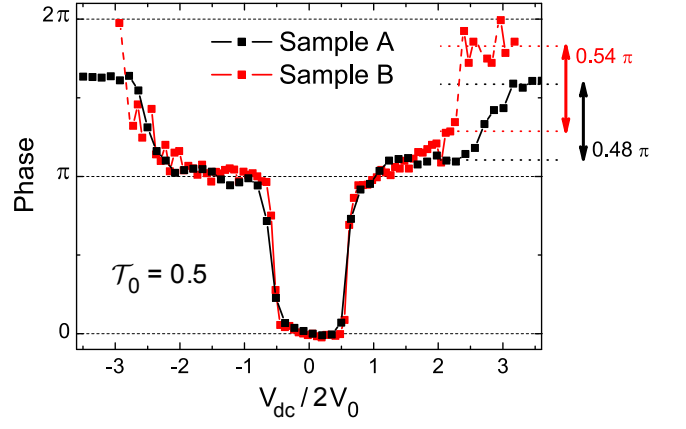

FIG. S10. **AB-phase evolution at the phase transition:** For $\mathcal{T}_0 = 0.5$ (measured for $V_{\mathrm{dc}} = 0$) multiple side lobes are observed for sample A. In sample B only single side lobes are visible with a width similar to $\mathcal{T}_0 > 0.5$. The phase evolution shows in both samples a jump of π at the first node. In sample A we clearly see a further increase of the phase that saturates near $3\pi/2$. The second side lobes are pronounced. Sample B shows a similar unexpected behavior.

visibility node a further gradual shift of the phase towards higher values can be clearly seen. The additional phase shift saturates at $\pi/2$ for sample A. In sample B only residual traces of an additional side lobe are visible, which also do not obey phase rigidity. The fact that multiple side lobes are observed near $\mathcal{T}_0 = 0.5$ may be explained by a variation of $\mathcal{T}_0$ with V_{dc} that are consistent with the observed non-linearities of the QPCs of sample A,[9] and result in a transmission $\mathcal{T}_0$ at finite V_{dc}, which slightly increases with V_{dc}. On the other hand, the deviations from phase rigidity observed in Fig. S10 cannot be understood in this way.

IV. THEORETICAL METHOD

In the main part of the paper, we present an explanation of the lobe-type pattern of visibility in electronic MZI in simple physical terms. A more rigorous description of QH interferometers at filling factor 2, proposed in Ref. 6, is based on the so-called bosonization approach. Here, we summarize this approach in order to support the elementary derivation given in the main part of the paper. For simplicity, we set $e = \hbar = 1$ in the beginning and restore physical units at the end of calculations.

Our experiment addresses the physics of MZIs at low-energies compared to the Fermi energy and at long distances compared to the magnetic length. The low-energy spectrum of excitations of chiral edge states consists of the collective charge density oscillation (plasmons). Using second quantization language, these excitations are described by creation and annihilation operators, satis-

fying the bosonic commutation relations

$$[a^{\dagger}_{s\alpha k}, a_{s'\beta k'}] = \delta_{ss'}\delta_{\alpha\beta}\delta_{kk'}, \qquad \text{(S11)}$$

where $s = 1, 2$ enumerates two arms of the interferometer, $\alpha = 1, 2$ enumerates two Landau levels at filling factor 2, and k is the wave vector. Namely, 1D charge densities may be expressed as

$$\rho_{s\alpha}(x) = (1/2\pi)\partial_x\phi_{s\alpha}(x) \qquad \text{(S12)}$$

in terms of boson fields

$$\phi_{s\alpha}(x) = \varphi_{s\alpha} + 2\pi N_{s\alpha}x/W \qquad \text{(S13)}$$
$$+ \sum_{k>0}\sqrt{2\pi/kW}(e^{ikx}a_{s\alpha k} + e^{-ikx}a^{\dagger}_{s\alpha k}),$$

which satisfy the canonical commutation relations $[\partial\phi_{s\alpha}(x), \phi_{s'\beta}(y)] = 2\pi i\delta_{ss'}\delta_{\alpha\beta}\delta(x-y)$. Here, W is the total size of the system (to be taken to infinity in the end of calculations), and the operators $\varphi_{s\alpha}$ and $N_{s\alpha}$ are the so-called zero modes, i.e, the modes with $k = 0$: $N_{s\alpha} = \int dx\rho_{s\alpha}(x)$ is the total number of electrons in the channel (s, α), and operators $\exp[-i\varphi_{s\alpha}]$ increases this number by 1.

The key idea of the bosonization technique is to express the electron creation operators in terms of the boson fields:

$$\psi^{\dagger}_{s\alpha}(x) = \exp[-i\phi_{s\alpha}(x)]. \qquad \text{(S14)}$$

With the help of Eqs. (S11-S14) one can check that (i) so-defined operators obey *fermionic* anti-commutation relations; (ii) they create local excitations with unit charge, i.e., they commute with charge density operators as $[\rho_{s\alpha}(x), \psi^{\dagger}_{s\alpha}(y)] = \delta(x-y)\psi^{\dagger}_{s\alpha}(x)$. When acting on the state of the interferometer, such operator first increases the total number of electrons $N_{s\alpha}$ by one, and second, it creates a bunch of plasmon excitations localized near the point x, as can be easily seen from Eq. (S14). These two effects are reflected in Eq. 2 in the main text.

The convenience of the bosonization approach is in the fact that the Hamiltonian of interacting 1D electrons is quadratic in terms of the boson fields and can be easily diagonalized. In particular, it has been shown in Ref. 6 that the Hamiltonian of electrons interacting via the short-range potential $U(x, y) = U\delta(x-y)$ can be written as:

$$\mathcal{H} = \frac{1}{2}\sum_{s,\alpha,\beta}\int_0^W dx V_{\alpha\beta}\rho_{s\alpha}(x)\rho_{s\beta}(x), \qquad \text{(S15)}$$

where the inverse "capacitance" matrix $V_{\alpha\beta} = U + 2\pi v_F\delta_{\alpha\beta}$ contains the Fermi sea contribution with the Fermi velocity v_F. It is easy to see that this Hamiltonian can be rewritten in the diagonal form:

$$\mathcal{H} = \int_0^W \frac{dx}{4\pi}\left[u(\partial_x\tilde{\phi}_{s1}(x))^2 + v(\partial_x\tilde{\phi}_{s2}(x))^2\right] \qquad \text{(S16)}$$

in terms of the charge and dipole modes $\tilde{\phi}_{s1,2}(x) = [\phi_{s1}(x) \pm \phi_{s2}(x)]/\sqrt{2}$. Note that the velocity of the charge mode $u = U/\pi + v_F$ is much larger then the velocity of dipole mode $v = v_F$ in the limit of the strong interaction $U \gg v_F$, which applies, e.g., for Coulomb interactions screened at relatively long distances. The new plasmon operators

$$\tilde{a}_{s1k} = \frac{1}{\sqrt{2}}(a_{s1k} + a_{s2k}), \ \tilde{a}_{s2k} = \frac{1}{\sqrt{2}}(a_{s1k} - a_{s2k}) \text{ (S17)}$$

have a simple physical meaning: They create and annihilate charge and dipole plasmon excitations with the wave vector k.

Next, we note that the zero mode contribution $\sum V_{\alpha\beta}N_{s\alpha}N_{s\beta}/2W$ to the Hamiltonian (S15) can be interpreted as an energy of a capacitor with capacitance matrix $W \cdot V_{\alpha\beta}^{-1}$. Using this fact one can find the average value of the charge operators in terms of electrochemical potentials $\Delta\mu_\alpha$. In particular, the total number of electrons in the upper outer channel reads: $N_{U1} = W\sum \cdot V_{1\alpha}^{-1}\Delta\mu_\alpha \simeq W\Delta\mu_1/4\pi v$, for $\Delta\mu_2 = 0$, and where we have neglected small contribution $\sim 1/u$. Thus, according to Eqs. (S14) and (S14), the excitations created by electron tunneling acquire the following phase from zero modes (restoring physical units and setting $\Delta\mu_1 = eV_{\text{dc}}$)

$$\delta\varphi_0 = -W\Delta\mu_1/4\pi\hbar v \cdot 2\pi L/W = -eV_{\text{dc}}L/2\hbar v, \quad \text{(S18)}$$

which explains Eq. 5 in the main text.

Let us now consider the dynamical phase acquired by the plasmons. From the Hamiltonian (S16) it follows that:

$$\tilde{a}_{s1k}(t) = e^{-iukt}\tilde{a}_{s1k}, \quad \tilde{a}_{s2k}(t) = e^{-ivkt}\tilde{a}_{s2k}. \quad \text{(S19)}$$

These relations determine the time evolution of the electron operator (S14). On the other hand, the wave function overlap introduced in the main part of the paper my be written as

$$\langle\psi_{N+1}|\psi'_{N+1}\rangle \propto \int dt e^{\Delta\mu_1 t}\langle N|\psi_{U1}(0,0)\psi^{\dagger}_{U1}(L,t)|N\rangle, \qquad \text{(S20)}$$

where the time integral projects an electron onto the energy $\Delta\mu_1$, with which it is injected. The similar contribution from the lower arm of the interferometer has been omitted for the sake of simplicity of the argument.

The complication in the next step arises because each electron operator on the right hand side of (S20) generates an infinite number of terms, when expanded in the plasmon operators, which can be schematically expressed as following: $\langle\psi_{N+1}|\psi'_{N+1}\rangle \propto \sum C_{\{k\}}C_{\{k'\}}e^{-i(K+K')L}\delta(\Delta\mu_1 + Ku + K'v)$, where $C_{\{k\}}$ and $C_{\{k'\}}$ are the plasmon correlation functions for the sets of wave numbers k_i and k'_i, and $K = \sum_i k_i$, $K' = \sum_i k'_i$. Here we have used Eqs. (S14), (S14), (S19), and integrated over time t to obtain the energy conserving delta-function. It is easy to see that in the large-L limit the summation over all possible plasmon excitations leads to fast oscillations in the above expression

and to the suppression of corresponding contributions. However, two terms in this sum, the separate contributions of the dipole and charge mode, constitute an exception: $\langle\psi_{N+1}|\psi'_{N+1}\rangle \propto \sum C_{\{k\}}e^{-iKL}\delta(\Delta\mu_1 + Ku) + \sum C_{\{k'\}}e^{-iK'L}\delta(\Delta\mu_1 + K'v)$. Thus, as a consequence of the linear spectrum of plasmons (and of the chirality of the system), we immediately arrive at the expression $\langle\psi_{N+1}|\psi'_{N+1}\rangle \propto e^{i\Delta\mu_1 L/u} + e^{i\Delta\mu_1 L/v}$, which justifies our simplified approach in the main part of the paper, leading to Eq. (4). In the limit $u \gg v$, restoring physical units and setting $\Delta\mu_1 = eV_{\text{dc}}$, the relative phase shift due to the dipole mode reads

$$\delta\varphi_{\text{d}} = eV_{\text{dc}}L/\hbar v. \tag{S21}$$

Note, that the universality of the ratio $\delta\varphi_{\text{d}}/\delta\varphi_0 = -2$, which follows from strong interactions at QH edge, explains the origin of the phase rigidity and phase transition phenomena observed in our experiment.

V. NUMERICAL RESULTS FOR GAUSSIAN AND NON-GAUSSIAN NOISE VERSUS EXPERIMENTAL DATA

In the main part of this work we illustrated the qualitative signatures of the phase transition when going from $\mathcal{T}_0 > 0.5$ to $\mathcal{T}_0 < 0.5$. Here we want to go more into detail of the expected differences in the visibility characteristics predicted for Gaussian and non-Gaussian noise. In Fig. S11 we compare two traces of $\nu(V_{\text{dc}})$ for $\mathcal{T}_0 = 0.5$ and $\mathcal{T}_0 = 0.4$ with the results of the numerical calculations described in the following.

Ref. 5 provides analytically-derived large-bias asymptotics of the visibility of AB oscillations in Gaussian and non-Gaussian regimes. These asymptotics are based on the Levitov-Lesovik formula[7] for the long-time behavior of the FCS generator of tunneling currents at the QPC0. However, large-bias asymptotics are not sufficient for a direct comparison with our experimental results. For this reason, we follow the approach proposed in Ref. 5 and evaluate the FCS generator numerically. To this end we use the determinant representation of the FCS generator (see Refs. 7 and 10) which allows one to express this generator as a determinant of a single-particle operator:

$$\langle e^{i\lambda N(t)}e^{-i\lambda N(0)}\rangle =$$
$$\det[1 - f(\varepsilon) + \exp(i\lambda U(t) \otimes S(\varepsilon))f(\varepsilon)], \tag{S22}$$

where $f(\varepsilon)$ is the energy distribution function, $U(t)$ is the projector on the time interval $[0,t]$, and $S(\varepsilon)$ is the scattering matrix of the QPC0.

We introduce a finite bandwidth for the electrons in the incoming channels of QPC0 and fix it to be 4000 times larger than the level spacing. Thus, we reduce the problem of finding the FCS generator to the evaluation of the determinant of a finite matrix of the size 4000 by 4000. The evaluation of such a determinant as a function of time t and of the transparency $\mathcal{T}_0$ can be trivially
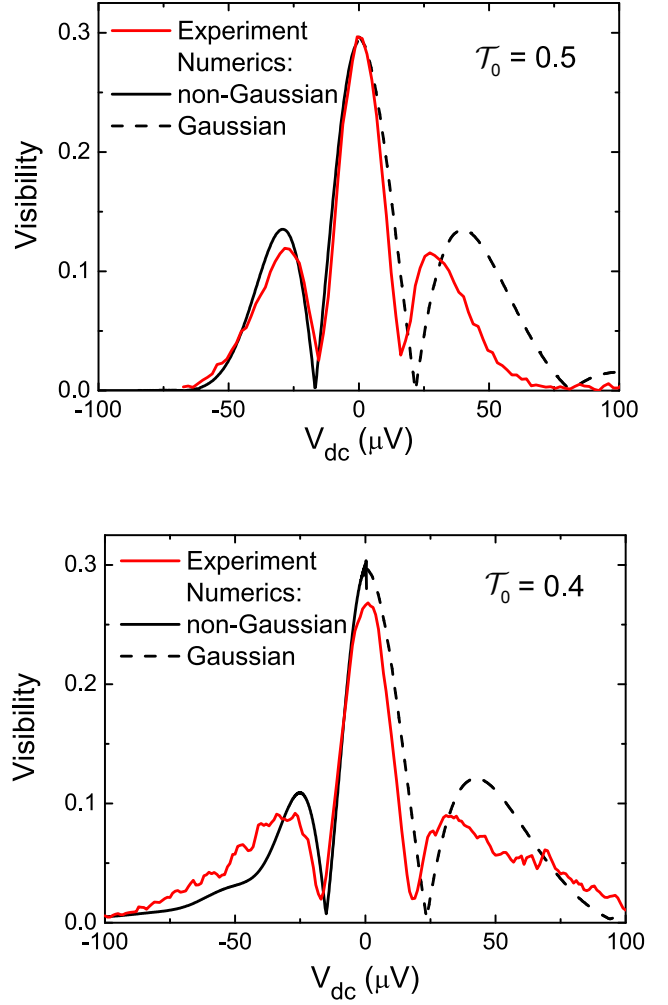

FIG. S11. **Comparison to theory** for $\mathcal{T}_0 = 0.5$, and $\mathcal{T}_0 = 0.4$ of sample B. In the fits of Gaussian (right half of graphs) and non-Gaussian (left half of graphs) noise the only free parameters are ν_0 and V_2 at $\mathcal{T}_0 = 1$. The better agreement to the non-Gaussian prediction is obvious.

parallelized and has been done using the Blue Gene/P machine[11]. Then, we evaluate numerically the integral in the Eq. 3 of Ref. 5, which connects the visibility and the FCS generator via Eq. 7 of Ref. 5, and find the visibility as a function of the voltage bias and of the transparency.

To compare this numerical data to the experiment we determine ν_0, from the data of $\mathcal{T}_0 = 1$, and the position of the 2nd node V_2 at $\mathcal{T}_0 = 1$ as in Fig. 4 in the main part. Fig. S11 shows the bias dependent visibility for $\mathcal{T}_0 = 0.5$ and 0.4 in sample B with the numerical calculation for Gaussian and non-Gaussian noise. As one can see the nodes for the Gaussian prediction are expected for larger voltages as in the measurement and an additional side lobe should be present with a height that should be measureable. The curve for the non-gaussian prediction fits much better and the only small discrepancy is the height

of the side lobe. This observation suggest again a strong, almost diverging, dephasing characteristic for the non-Gaussian noise distribution expected after QPC0. The situation is similar for $\mathcal{T}_0 = 0.4$ – multiple side lobes and position of nodes of the Gaussian prediction do not fit the measurement.

In conclusion, the two parameters ν_0 and V_0 deter-mined independently at $\mathcal{T}_0 = 1$ fix the whole set of visibility curves calculated for Gaussian and non-Gaussian noise at different $\mathcal{T}_0$. The experimental data agree much better with the non-Gaussian than with the Gaussian curves for all transmissions $\mathcal{T}_0$. This provides striking evidence for the noise-induced phase transition proposed in Ref. 5.

---

[1] L. V. Litvin, H.-P. Tranitz, W. Wegscheider, and C. Strunk, Phys. Rev. B **75**, 033315 (2007).

[2] L. V. Litvin, A. Helzel, H.-P. Tranitz, W. Wegscheider, and C. Strunk, Phys. Rev. B **78**, 075303 (2008).

[3] M. Hashisaka, A. Helzel, S. Nakamura, L. V. Litvin, Y. Yamauchi, K. Kobayashi, T. Ono, H.-P. Tranitz, W. Wegscheider, and C. Strunk, Physica E **42**, 1091-1094 (2010).

[4] P. Roulleau, F. Portier, P. Roche, A. Cavanna, G. Faini, U. Gennser, and D. Mailly, Phys. Rev. Lett **100**, 126802 (2008).

[5] I. P. Levkivskyi, and E. V. Sukhorukov, Phys. Rev. Lett. **103**, 036801 (2009).

[6] Ivan P. Levkivskyi, Eugene V. Sukhorukov, Phys.Rev. B **78**, 045322 (2008).

[7] L. S. Levitov, H. Lee, and G. B. Lesovik, J. Math. Phys. **37**(10), 4845 (1996).

[8] I. P. Levkivskyi, and E. V. Sukhorukov, Phys. Rev. B **85**, 075309 (2012).

[9] L. V. Litvin, A. Helzel, H.-P. Tranitz, W. Wegscheider, and C. Strunk, Phys. Rev. B **81**, 205425 (2010).

[10] N. N. Bogoliubov, D. V. Shirkov, *Quantum Fields* (Benjamin-Cummings Pub. Co, 1982).

[11] http://bluegene.epfl.ch/